Post-Earthquake Fold Growth Imaged in the Qaidam basin, China, With InSAR

Simon Daout[1], **Barry Parsons**[1], **Richard Walker**[1]

[1]COMET, Department of Earth Sciences, University of Oxford, UK

Key Points:

- 16-years of post-seismic transient deformations measured with InSAR.
- Spatio-temporal changes of post-seismic rates and patterns have been observed.
- Distributed fold buckling triggered by underlying fault slip has been interpreted.

Corresponding author: Simon Daout, simon.daout@earth.ox.ac.uk

Abstract

Questions regarding the development of folds and their interactions with the seismic faults within thrust systems remain unanswered. However, estimating fault slip and earthquake hazards using surface observations and kinematic models of folding requires an understanding of how the shortening is accommodated during the different phases of the earthquake cycle. Here, we construct 16-years of InSAR time series across the North Qaidam thrust system (NE Tibet), where three Mw 6.3 earthquakes occurred along basement faults underlying shortened folded sediments. The analysis reveals spatio-temporal changes of post-seismic surface displacement rates and patterns, which continue more than ten years after the seismic events. The decomposition of the Sentinel-1 ascending and descending LOS velocities into vertical and shortening post-seismic components indicates that long-term transient uplift and shortening coincide spatially with young anticlines observed in the geomorphology and cannot simply be explained by elastic slip along dislocations. These findings provide evidences for fold buckling during the post-earthquake phase and highlight the contribution of distributed aseismic deformation to the growth of topography.

1 Introduction

Numerous studies have observed that folds grow primarily due to slip on underlying faults and that their surface expressions, such as anticline geometries, can be used directly to infer long-term fault slip rates (e.g., Suppe, 1983; Ward & Valensise, 1994; Shaw et al., 2002, 2005; Daëron et al., 2007; Dolan & Avouac, 2007; Brandes & Tanner, 2014; Guilbaud et al., 2017). However, the importance of fold buckling and distributed strain to the component of shortening and fold growth is not clear (e.g., Gonzalez-Mieres & Suppe, 2006; Yonkee & Weil, 2010; Veloza et al., 2015; Ainscoe et al., 2017). In other words, it is also recognised in the literature that there is not a simple relationship between slip and fold growth (e.g., Huang & Johnson, 2016; Bonanno et al., 2017; Johnson, 2018).

Some studies have used geodetic measurements of coseismic surface displacements to document growth of anticlines (e.g., Stein & King, 1984; Nissen et al., 2007; Belabbès et al., 2009; Tizzani et al., 2013). However, recent satellite-based measurements have highlighted the observation that the surface ground deformation associated with thrust earthquakes often does not match the present-day or Quaternary active geomorphology in extent and that it is unlikely that repeated earthquakes of the same type could reproduce the observed topography (e.g., Copley, 2014; Mackenzie et al., 2016; Elliott et al., 2016; Ainscoe et al., 2017; Barnhart et al., 2018). In addition, although simplified models are

valuable in many ways, modelling shortening and the associated uplift across a fold-and-thrust belt system with one or two elastic dislocations is an arguable simplification of the complicated history and geometry of a thrusting morphology, which may involve several interconnected faults and folds that interact with each other, multiple bends, and anelastic deformation as in the upper plate around the bends (e.g., Davis et al., 1983; Tapponnier et al., 1990; Medwedeff & Suppe, 1997; Daout et al., 2016; Whipple et al., 2016; Sathiakumar et al., 2020). Some other geodetic observations have recently documented or/and modeled episodic aseismic ground deformations (e.g., Mariniere et al., 2020) or long-periods of afterslip that correlate with the present-day geomorphology of fold-and-thrust belts (e.g., Fielding et al., 2004; Barnhart et al., 2013; Copley, 2014; Elliott et al., 2015; Mackenzie et al., 2016; Wimpenny et al., 2017; Zhou et al., 2018; Daout et al., 2019). These measurements suggest that the permanent deformation in fold-and-thrust belts might be sometimes created by distributed off-fault deformation (i.e volumetric plastic deformation), or aseismic slip on secondary faults branching from the main earthquake fault or around it, and which occur during stages of the earthquake cycle other than the seismic event. Despite the likely importance of those phenomena, little is known about the link between seismic slip on the main fault and slip on secondary faults or distributed deformation following a seismic event. To understand how topography is generated by repeated earthquake cycles and/or by other processes, and to constrain the period within the earthquake cycle during which geomorphological structures are formed, it is necessary, therefore, to bridge the discrepancy between simple geodetic models of fault slip and geological models of fold-and-thrust belts, by combining measurements of surface displacements over a long-time period and with realistic structural fold-and-fault geometries.

The North Qaidam thrust (NQT) system is located at the southernmost part of the Qilian Shan-Nan Shan thrust belt and exhibits segmented anticlines striking in a northwest-southeast direction (Fig. 1). In this NE part of the Tibetan Plateau, while major strike-slip faults, such as the Kunlun and Haiyuan Faults, have received considerable attention from the tectonic and geodetic communities, data from the thrust systems in the South Qilian Shan are not widely reported, and little is known about the structural geology of the region (e.g., Meyer et al., 1998; Fang et al., 2007; Yin, Dang, Wang, et al., 2008; Yin, Dang, Zhang, et al., 2008; Tapponnier et al., 2001; Guihua et al., 2013). According to sparse GNSS measurements, about 4-6 mm/yr of convergence is accommodated there in an overall N22°E direction (Liang et al., 2013; Wang et al., 2017). The region is marked by active seismicity with three M_w 6.3 events occurring in a 150 km along-strike area between 2003 and 2009 (Fig. 1). The 17^{th} April 2003 Delingha earthquake ruptured part of the Zongwulong thrust with a centroid depth, derived from local seis-

mic network, of 16 km (Sun et al., 2012), in a section of the North Qaidam Shan which was previously unrecognised as active. It was followed by extensive and long-lasting logarithmic post-seismic slip that coincided with the Delingha anticline and continued into 2011 along a north-dipping creeping structure (Daout et al., 2019). As reported by the authors (Daout et al., 2019), shallow creep is in agreement with a rate-strengthening fault behavior of the uppermost part of the crust, but the duration and the spatial extent of the observed surface displacements following the 2003 earthquake, during the 2003-2011 Envisat period, is a notable particularity, despite the low strain rate of the area. The 10^{th} November 2008 and the 28^{th} August 2009 Haixi earthquakes occurred in close proximity to each other within the Olongbulak Shan, to the west of the Delingha rupture (Fig. 1), and were followed by a period of an increased rate of seismicity in the region and aseismic slip (Elliott et al., 2011; Guihua et al., 2013; Feng, 2015; Liu et al., 2015; Liu, Xu, Wen, & Li, 2016; Liu, Xu, Li, et al., 2016; Daout et al., 2019; Daout, Steinberg, et al., 2020). Daout, Steinberg, et al. (2020) modelled the 2008 earthquake with a $\sim$32° north-dipping fault that roots under the Olongbulak pop-up structure at $\sim$12 km depth (top edge of the fault), as well as downdip aferslip along a coplanar north-dipping plane. They also inferred three south-dipping segmented $\sim$55-75° high-angle faults for the 2009 earthquake with fault tip depths between $\sim$2.5-4.5 km and three post-seimic faults with similar geometries than the three earthquake patches (Daout, Steinberg, et al., 2020). They, therefore, inferred a low-angle north-dipping décollement that roots at the bottom of the fold-and-thrust belt structures of the NQT transferring the shortening rate from the north, along the Qilian Shan, to the south, in the Qaidam basin, in agreement with the southward expansion of the South Qilian Shan since the Neogene (Pang et al., 2019)(Fig. 1b).

In this study, we conduct a MT-InSAR analysis across this northeastern part of the Tibetan Plateau using both C-band Envisat (2003-2011) data derived from Daout et al. (2019), and C-band Sentinel-1 (2014-2019) data (Figs. 1, S1). We processed the Sentinel-1 data set and corrected both Envisat and Sentinel-1 data sets for tropospheric path delays using the newly ERA-5 atmospheric model provided by ECMWF. To capture and quantify the spatio-temporal change of the aseismic strain release that follow the 2008-2009 Haixi (Fig. 3) and 2003 Delingha (Fig. 2) earthquakes, we extract linear ground velocities over different time spans with a parametric decomposition. We then decompose both ascending and descending LOS velocities into an N22°E horizontal velocity, which is the main direction of shortening, perpendicular to the overall orientation of the North Qaidam thrust systems, and a vertical surface velocity (Figs. 5, 4), to infer two structural models of the folds and associated faults for the two areas.

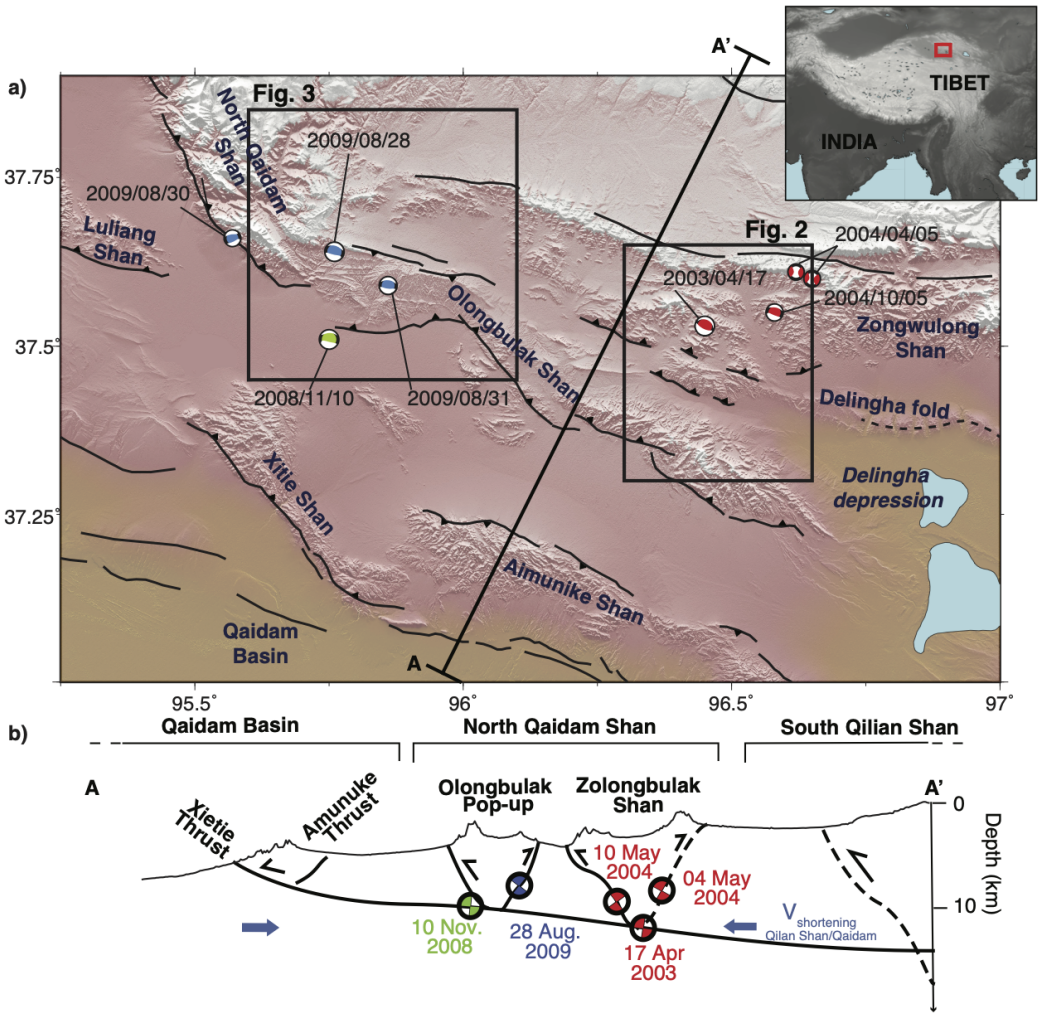

Figure 1. a) Seismotectonic setting of the northeastern part of the North Qaidam thrust system with fault traces and focal mechanisms of the 8 M_w >5.2 events (USGS catalogue) that occurred within the Olongbulak and Zongwulong ranges from 2003 to 2009. Topography is from the SRTM 30 m hill-shaded Digital Elevation Model. Top right inset: regional setting and location of the study area (red box). b) Topography profile marked AA' in (a) with a regional conceptual interpreted fault structures and earthquake locations derived from Daout et al. (2019), Daout, Steinberg, et al. (2020), and the available cross-sections of Yin, Dang, Wang, et al. (2008), Fang et al. (2007), and Guihua et al. (2013).

2 Data and Method

2.1 InSAR data processing

We used the three Envisat time series data along five ∼300-km-long and 100-km-wide overlapping tracks (descending tracks 319, 047, 276, 90 and ascending track 455) between 2003 and 2011, processed in Daout et al. (2019) (Fig. S2). Additionally, we processed three Sentinel-1 tracks (descending tracks 004 and ascending tracks 172 and 099) acquired in interferometric wide-swath mode (width of ∼250 km) from 2014 to 2019 (Fig. S2). The processing is carried out using the New Small Baselines Subset (NSBAS) processing chain (Doin et al., 2011, 2015), which includes routines from the ROI_PAC software (Rosen et al., 2004) and precise azimuthal coregistration with the spectral diversity technique for Sentinel-1 data (Grandin, 2015; Grandin et al., 2016; Métois et al., 2020). In order to avoid possible biases linked to the inclusion of short temporal baselines (Ansari et al., 2020), we include interferograms with both short and long temporal baselines in the analysis (Fig. S2) that we successfully unwrap by applying empirical atmospheric corrections before unwrapping and by imposing an unwrapping path that start from more coherent areas and expand progressively into lower coherence (Grandin et al., 2012).

After unwrapping, we re-introduce the empirical corrections that had been applied on the wrapped phase and construct cumulative time series on a pixel-by-pixel basis with the NSBAS method (López-Quiroz et al., 2009; Doin et al., 2015). Residual unwrapping errors are first detected by visual inspection on interferograms or with high phase misclosure computed from the time series analysis (López-Quiroz et al., 2009; Doin et al., 2011). Errors are then corrected by imposing high-priority paths during a new unwrapping iteration. As part of the time series analysis, remaining unwrapping errors are further automatically identified and resolved using an iterative technique (López-Quiroz et al., 2009). In order to improve the referencing estimation and exclude surface periglacial processes from this analysis, we then, mask all pixels showing in the timeline of ground deformation, seasonal displacements higher than 3,5 mm associated with frost heave and thaw settlement of the permafrost active layer (Daout, Dini, et al., 2020). Cumulative LOS displacements (LOS(t)) from both Envisat and Sentinel-1 data are, subsequently corrected for tropospheric effects using the ERA-5 atmospheric model provided by ECMWF (Doin et al., 2009; Jolivet et al., 2011), and referred to an 100×100 pixels area within the Qaidam basin of low elevation, low deformation gradient and high coherence. Afterwards, in order to map and quantify the spatio-temporal strain evolution and associated uncertainties, we proceed to a simple linear parametric decomposition of the co-seismic and post-seismic ground deformations for the two earthquake areas.

2.2 Parametric decomposition

Sentinel-1 tracks 004, 172 and 099 are first decomposed, assuming zero displacement during the first acquisition, into a single linear trend from 2014 to 2019 ($V_{2014-2019}$ in mm/yr) in both rupture areas (Fig. S3):

$$LOS_{14-19}(t) = V_{14-19}t, \tag{1}$$

where t is the SAR acquisition time. As the 28^{th} August 2009 Haixi earthquake was imaged by the Envisat descending track 319, we impose for this time series two basis functions:

$$LOS_{09-11}(t) = V_{09-11}t + A_{09} * H(t - t_{09}), \tag{2}$$

where t_{09}, the timing of the 2009 earthquake; H, the Heaviside function; and A_{09} and V_{09-11} correspond to the amplitude of the August 2009 coseismic surface displacements (in mm) and the mean velocity from 2009 to 2011 (in mm/yr), respectively (Fig. 3). The 10^{th} November 2008 earthquake occurred south of the Olongbulak Shan with a depth of ∼12 km and produced short-term downdip afterslip over two times smaller than the 28^{th} August 2009 shallow event, which occurred at a depth of ∼5 km (Elliott et al., 2011; Daout, Dini, et al., 2020). Despite the deep origin of the 2008 post-seismic, it is important to note that the short-term post-seismic observed in the Envisat data during the 2009-2011 period, might be a combination of the post-seismic surface displacements from both Haxi earthquakes.

Independently, in order to quantify the spatio-temporal evolution of the post-seismic strain release after the 17^{th} April 2003 Delingha earthquake, we prescribe, for track 047, two linear trends from 2003 to 2006 (V_{03-06}) and from 2006 to 2011 (V_{06-11}) (Fig. 2):

$$LOS_{03-11}(t) \quad = V_{03-06}t \quad for \quad 2003 \leq t \leq 2006, \tag{3}$$

$$= V_{06-11}t \quad for \quad t > 2006 \tag{4}$$

By dividing the 2003-2011 time series data set into two distinct velocity periods, we avoid imposing any logarithmic or exponential post-seismic relationship on the data for descending track 047 (Fig. 2). However, due to the poor temporal resolution of ascending track 455 (9 acquisitions only for this track) and the presence of only 2 acquisitions after the August 2009 Haixi earthquake, we only prescribe a single linear trend

from 2003 to 2011 (V_{03-11}, in mm/yr) to extract the average strain rate around the Delingha earthquake area in ascending geometry (Fig. 2):

$$LOS(t) = V_{03-11}t. \tag{5}$$

2.3 Uncertainty estimations and comparison with GNSS

Two ascending and one descending Sentinel-1 track, with a total of 248 acquisitions, illuminate at a regional scale the LOS surface velocity from 2014 to 2019 over a 120,000 km^2 area of northeastern Tibet (Fig. S3). Uncertainty maps, derived from the time series decomposition (Fig. S4), are of 0.6 [0.4−0.8] mm/yr on average (with 95% confidence intervals), with a maximum uncertainty of up to ∼2 mm/yr in Qilian and Kunlun high ranges or at the bottom of some localised valleys. Those average low uncertainties, as well as the good agreement of the data within the profile in the overlapping area of the two ascending track 099 and 172 validates the quality of the results (Fig. S5a). Histograms of differences of the overlap are approximatively Gaussian with mean close to zero and standard deviation of less than ∼0.5 mm/yr (Fig. S5b). Descending track 004 also shows a good agreement with the regional Envisat velocity map from 2003 to 2011 obtained in Daout et al. (2019) (Fig. S6). However, the histogram of differences has an higher standard deviation for Envisat data, which can be explained by the larger noise of this data set due to the poorer temporal sampling in comparison to Sentinel-1 data and to the difference in time span. Velocity maps also show some high velocity gradients towards the satellite in many basins bounded by high ranges, where uncertainties are also higher. Because interferograms have been corrected using the ERA-5 atmospheric model, and because of the good agreement between adjacent ascending tracks and the descending Envisat and Sentine-1 velocity maps, we discard large tropospheric residual signals (>∼1mm/yr) in the velocity maps that arise from the oddly sampled seasonal stratified delays (Doin et al., 2009; Daout et al., 2018). We associate the apparent correlation with the topography as due to the effect of a long-term increase of water content within the sedimentary basins. Those InSAR observations are in agreement with the water mass increase and gradual expansion of water levels of many lakes of North-East and Central Tibet of the past few decades, amplified by increase in surface air temperature and precipitation, melting of glaciers and thawing of ice-rich permafrost (Bibi et al., 2018; Daout, Dini, et al., 2020).

3 Results: Observational Constraints

To first-order, the LOS velocity maps (Fig. S3) show, for both ascending and descending tracks, relative displacements away from the satellite (negative values) from the southern front of the Qilian and Qilian-Nan ranges to the North Qaidam thrust systems (within the North Qaidam ranges), and displacements towards the satellite (positive value) within the Qilian or Qilian-Nan ranges and within the Qaidam Basin, likely associated with the N22°E ∼4-6 mm/yr of shortening across the whole region, derived from GNSS measurements (Liang et al., 2013; Wang et al., 2017). Smaller-wavelength LOS gradients are correlated with Quaternary active fold-and-thrust belts on localised areas of the Qaidam Basin (Yin, Dang, Wang, et al., 2008; Yin, Dang, Zhang, et al., 2008) as across the Lenghu Anticlinorium, the south-dipping Aimunike Thrusts and north-dipping Xitieshan thrusts, or the Olongbulak and Delingha ranges (Fig. S3). Assuming a tectonic origin for the deformation, the velocities are probably related to the slow aseimic shortening and uplift of segmented thrust faults and folds a few tens of kilometers long within the Qaidam basin. However, as the signals here are relatively small, we choose not to interpret them further. In the following sections, we will focus on the two major deformation signals of the velocity map in Fig. S3, which are linked to the post-seismic ground deformation following the 2003-2009 Qaidam earthquake sequence (Fig. 1).

3.1 Post-seismic deformation of the 2003 Delingha earthquake.

Decomposition of the Envisat time series of cumulative displacements for a 2003-2006 and 2006-2011 velocities (in mm/yr), as well as Sentinel-1 surface displacements into an average 2014-2019 velocity (in mm/yr), illuminate the evolution of the post-seismic deformation for the 2003 M_w 6.3 Delingha earthquake in descending (Fig. 2a) and ascending geometries (Fig. 2b). In both views, the post-seismic deformation evolves in time from the superposition of a 13 km-long and 6 km-wide sharp signal at the southern topographic front and a broader and long-wavelength signal, ∼10 km further north, between 2003 to 2011, to a deformation pattern essentially concentrated across the Delingha anticline, between 2014 to 2019 (Fig. 2a,b).

During the 2014-2019 period, both ascending and descending LOS surface displacements highlight a sharp signal of up to ∼1.5 mm/yr that coincides with the topographic front of the Delingha anticline, in agreement with shallow deformation processes (Fig. 2a,d). In comparison with the descending view, the peak of the ground deformation in ascending view is shifted a few kilometres southward (Fig. 2d). This apparent difference in the peak of velocity gradient is likely due to the ∼NS shortening sensitivity difference between the two geometries, which will be extracted in the following section.

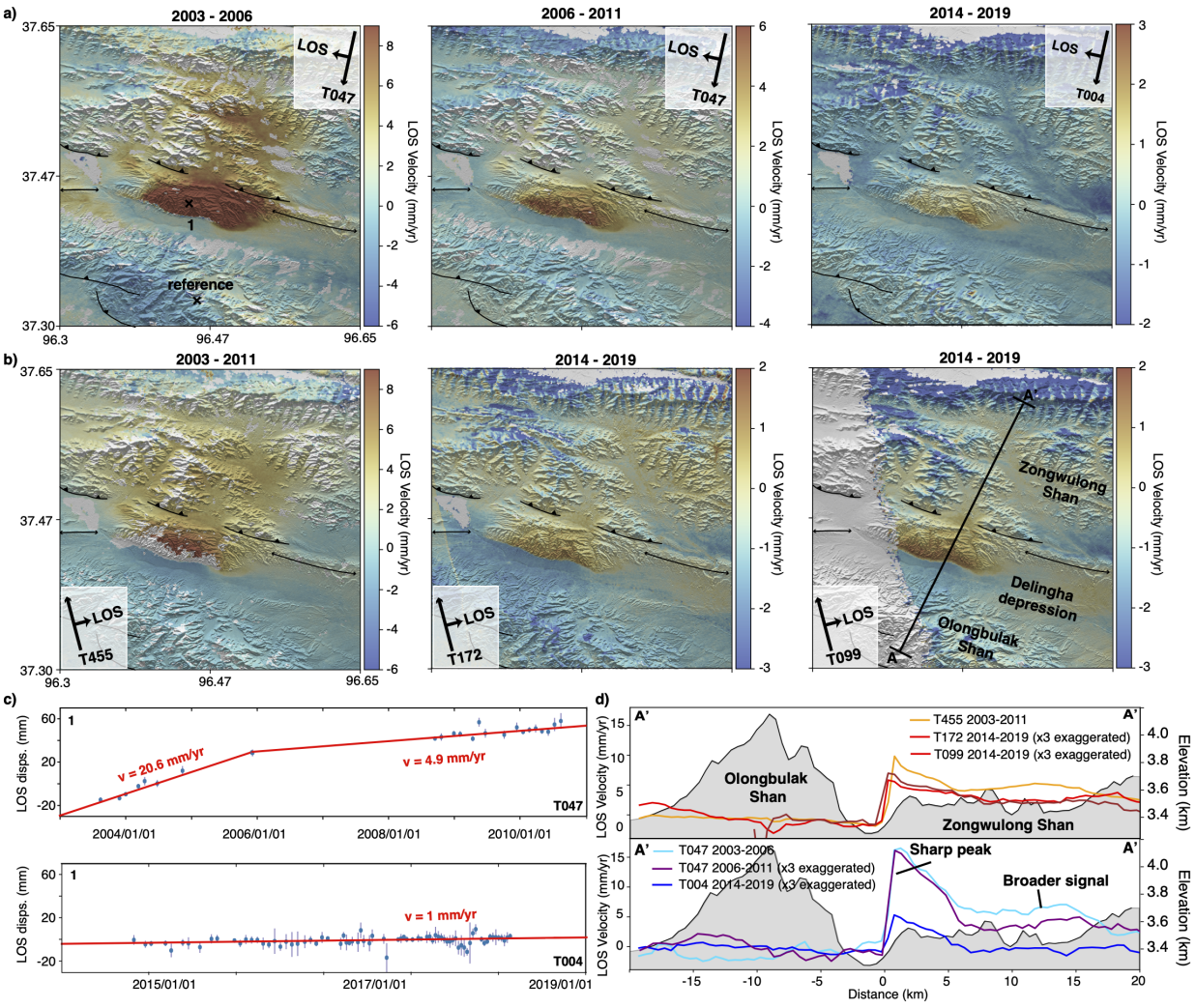

Figure 2. Post-seismic ground deformation following the 2003 Delingha earthquake. a) Velocity maps for the 2003-2006 period extracted from Envisat descending track 047 (left), for the 2006-2011 period extracted from Envisat descending track 047 (middle), and for the 2014-2019 period extracted from Sentinel-1 descending track 004 (right). b) Same as panel (a) but for the 2003-2011 period extracted from Envisat ascending track 455 (left), for the 2014-2019 period extracted from Sentinel-1 ascending track 172 (middle) and for 2014-2019 period extracted from Sentinel-1 ascending track 099 (middle). c) Time series displacements from 2003 to 2011 (top), determined using Envisat SAR data, and from 2014 to 2019 (bottom), from Sentinel-1 SAR data, for the pixel marked by a cross in (a) on the two descending tracks 047 and 004. d) Top: 40 km-long and 4 km-wide LOS profiles, marked AA' in panel (b), extracted through the Envisat ascending velocity map for 2003-2011 (orange lines) and the Sentinel-1 ascending velocity maps for 2014-2019 (red and brown lines). Bottom: Same LOS profile, but extracted through the Envisat descending velocity map from 2003-2006 (cyan lines), the Envisat descending velocity map from 2006-2011 (purple lines) and the Sentinel-1 descending velocity map from 2014-2019 (blue lines). Note that for comparison the Sentinel-1 velocities and the 2006-2011 Envisat velocities are 3 times vertically exaggerated.

While surface displacements are in good agreement with a logarithmic decay during the 2003-2011 period (Fig. 2c, (Daout et al., 2019)), Sentinel-1 measurements suggest deformation rates do not follow a $\frac{1}{t}$ decay, expected for deformation due to afterslip (e.g., Zhou et al., 2018). To get further insights about the deformation mechanisms, we compute the two-dimensional surface displacements for one 35° north-dipping and 20 km-long edge dislocation embedded in an elastic half-space with variable locking depths (LD = 0 km, 5 km or 10 km) in Fig. S8. The modeling results show that the measurements are in close agreement with a north-dipping thrust fault that riches the surface (LD=0 km). However, the very small amount of deformation in ascending and descending geometries detected in the footwall of the north-dipping structure both in map view (Fig. 2a) and along with the profile (Fig. 2d), differs from what might be expected for afterslip along a shallow elastic dislocation.

3.2 Post-seismic deformation of the 2009 Haixi earthquake.

Decomposition of the Envisat time-series of cumulative surface displacements into a coseismic step in 2009 (in mm) and an average 2009-2011 velocity (in mm/yr), as well as the Sentinel-1 surface displacements into an average 2014-2019 velocity (in mm/yr), illuminate the spatio-temporal evolution of the 2009 Haixi post-seismic strain release (Fig. 3a, Fig. S9). A spatial pattern similar to the 2009 Haixi earthquake is observed during the 2009-2011 aseismic period with Envisat, but extending slightly further north, as expected from shallow afterslip (Fig. 3a,c, Fig. S9). During this short period after the earthquake, rates are 1-6 cm/yr in the hanging wall of the south-dipping fault that broke in 2009, with a sharp and narrow maximum peak in the northwestern part, and −1-0 cm/yr, in a restricted area of the footwall of the south-dipping thrust (Fig. 3). The 2009-2011 short-term post-seismic velocities show an along-strike segmentation of the strain release, which can also be modeled with three south-dipping thrust-fault (Elliott et al., 2011; Daout, Steinberg, et al., 2020).

The 2014-2019 surface velocity maps in ascending and descending views, show surface displacements patterns that differ from the Envisat measurements from 2009 to 2011, with lobes towards the satellite matching almost perfectly the recent geological structures of the Olongbulak Shan observed in satellite imagery (Fig. 3a). For the descending geometry, a maximum surface LOS velocity of 4-5 mm/yr is measured on the northwestern part of the uplifted ranges, at the contact between the Paleozoic bedrock in the north, and the deformed sedimentary sequences of the Olongbulak Shan (Yin, Dang, Wang, et al., 2008; Guihua et al., 2013). The descending western profile there (blue line in profile AA' of Fig. 3c), suggests steep and asymmetric surface velocities with 2-3 mm/yr of

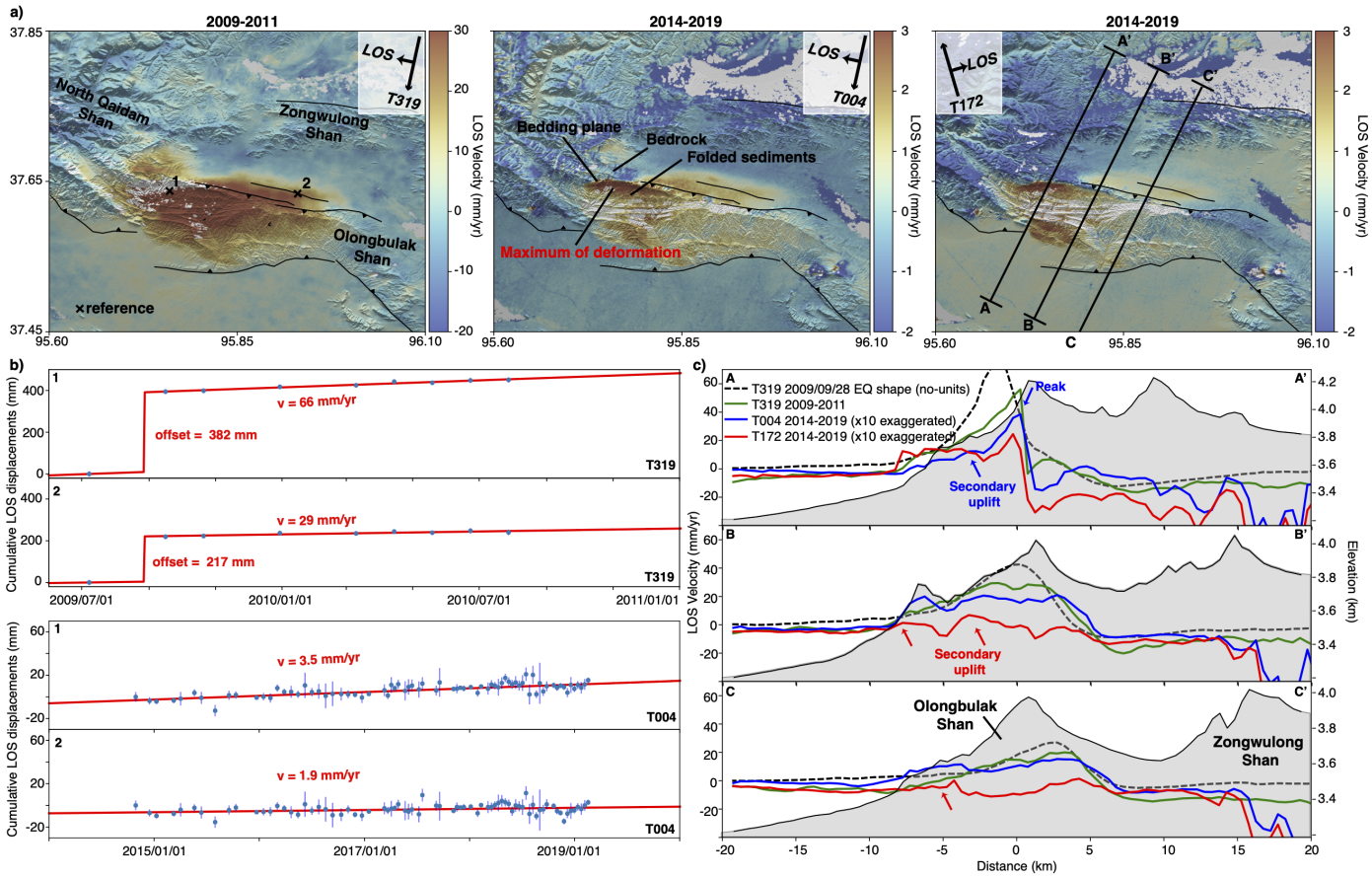

Figure 3. Post-seismic ground deformation following the 2009 Haixi earthquake. a) Velocity maps for the 2009-2011 period extracted from Envisat descending track 319 (left), for the 2014-2019 period extracted from Sentinel-1 descending track 004 (middle) and for the 2014-2019 period extracted from Sentinel-1 ascending track 172 (right). b) Time series displacements from 2009 to 2011 (top), determined for Envisat on descending track 319, and from 2014 to 2019 (Bottom), estimated for Sentinel-1 on descending track 004, for two pixels marked by crosses in (a). c) Three 40 km-long LOS profiles, marked AA', BB' and CC' in panel (a), extracted from the Envisat descending velocity map from 2009-2011 (green lines), the Sentinel-1 descending velocity map from 2014-2019 (blue lines) and the Sentinel-1 ascending velocity map from 2014-2019 (red lines). The profiles are average over velocities in a swath of 4 km wide. Note that, for comparison, the Sentinel-1 velocities are 10 times vertically exaggerated. The reduced coseismic surface displacement (in mm) is also shown by dashed black line on the three profiles for comparison with the post-seismic velocities (in mm/yr).

subsidence in the footwall. Positive surface velocities in the hanging wall of the Sentinel-1 data (blue profile in Fig. 3c) are slightly more distributed than in the 2009-2011 Envisat profile (green profile in Fig. 3c), with secondary lobes 2.5 km south of the maximum peak. The ascending profile (red profile in Fig. 3c), shows an even more distributed pattern, with a slower velocity peak of 2-3 mm/yr, in the northern front, shifted to the south in contrast to the descending geometry, and a ∼8 km-wide LOS pattern, in the NS direction, towards the satellite, which is correlated with the whole Olongbulak pop-up structure. On the two eastern profiles BB' and CC', post-seismic velocities during the 2014-2019 period are wider than the co-seismic surface displacements in both the two views, as for the 2009-2011 post-seismic velocities, but differ from the 2009-2011 period by showing additional short-wavelength peaks of LOS surface velocities towards the satellite in the southern part of the ranges. In other words, in contrast to the Envisat post-seismic measurements that suggest a single lobe of deformation that are in agreement with three shallow elastic high-angle faults (Fig. S8), Sentinel-1 observations indicate a more distributed signal, with deformation not only on the shallow northern part of the ranges, which broke during the 2009 event, but also across discrete sections of the southern part of the Olongbulak Shan.

4 Discussion

4.1 Inferred structural and kinematic models.

Both the Olongbulak and Delingha ranges have complicated surface expressions with both north-dipping and south-dipping scarps and with topography modified by erosion. Structural interpretations are, therefore, difficult for both areas, as illustrated by the variety of interpretations found in the literature (Fang et al., 2007; Yin, Dang, Wang, et al., 2008; Guihua et al., 2013). Geodetic measurement of surface displacements represent a good opportunity to show the utility of InSAR in elucidating structural models of fault-and-fold geometries. Decomposition of the LOS velocity signal into a N22°E horizontal and a vertical velocity (Figs. 4, 5, with associated uncertainties in Figs S9 and S10) is possible if we assume no ground deformation in the direction perpendicular to the shortening (Wright et al., 2004), which is here a reasonable assumption given the absence of strike-slip motion. From this decomposition, we observe that vertical surface displacements appear to affect the whole Delingha anticline and Olongbulak structure (Figs. 4b, 5b). Maximum horizontal displacements rates of 0.5-1 cm/yr are higher within these two structures than in the surrounding areas of the North Qaidam thrust systems and higher than the average GNSS shortening rate of ∼4 mm/yr, which is distributed across the whole North Qaidam fault system (Liang et al., 2013; Wang et al., 2017), indicating that mea-

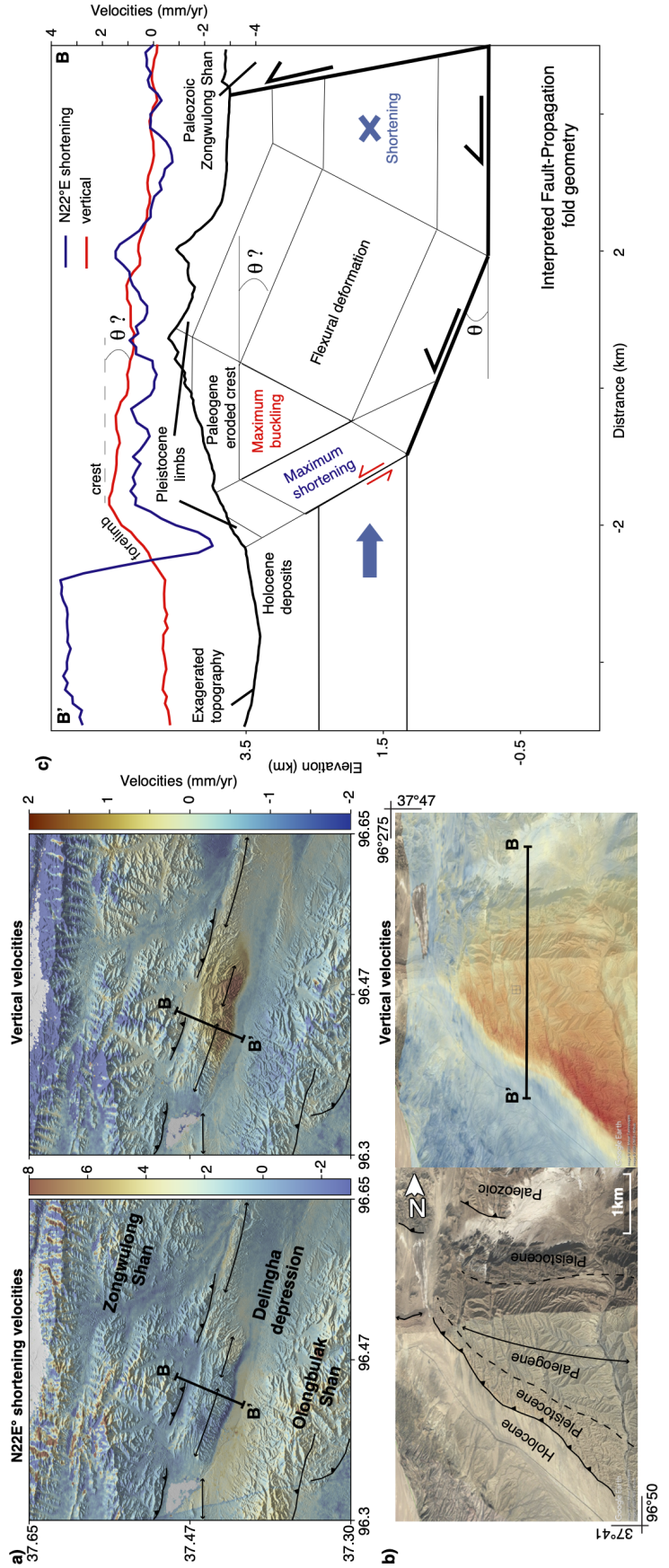

Figure 4. a) N22E shortening and vertical decomposition of the velocity of the Delingha earthquake area in Fig. 2 obtained from Sentinel-1 post-seismic LOS velocitiesfor ascending tracks 172 and 099 and descending track 004. Figure extend is as Fig. 2. b) Google-Earth imagery with interpreted geomorphological structures side-by-side with the enlargement of the vertical velocities of (a). Mapped active thrust faults are denoted by solid triangles in the hanging wall. The axes (black lines) and limbs (dashed lines) of the three anticlines are inferred from the geomorphology. c) Topography (black lines) and surface velocity profiles (N22°E shortening in blue, vertical in red) with interpreted structural cross-section sketches. Shortening gradients illuminate the inferred location of the tip of the blind thrusts and anticline forelimb, while maximal vertical gradients are located along the inferred folds crest and forelimb. We interpret the shortening and vertical post-seismic velocities as due to simple fault-propagation fold underlying the Delingha anticline.

sured surface displacement rates represent transient deformation induced by the earthquakes.

The structural cross-section across the Delingha anticline shown in Fig. 4c is inferred from the observed signal, our own geomorphological mapping, and available models from Yin, Dang, Wang, et al. (2008), Fang et al. (2007), and Daout et al. (2019). The Delingha fold shows sharp contacts between the truncated Pleistocene units on the southern sides of the fold and the Holocene deposits within the Delingha basin, in the footwall (Fig. 4b, (Yin, Dang, Wang, et al., 2008)). The exhumed Paleogene soft sediments in the core of the anticline (black lines in Fig. 4b) are light-coloured in comparison to the harder and more resistant uplifted Paleogene rocks exposed to the north and south of the anticline. We interpret the folding of the sedimentary beds to be caused by the fault step up over a ramp (Fig. 4c) (Walker, 2006). The geometry of the anticline is controlled by two kink bands, branching where the fault step up (kink 1 in Fig. 4c), and at the end of the fault tip (kink 2) (Suppe & Medwedeff, 1990; Brandes & Tanner, 2014). When the fault propagates, the beds roll from a flat position into the steep kink bands.

Daout et al. (2019) modeled the short-term logarithmic after-slip determined using Envisat data from 2003 to 2011 with a segmented ramp-flat-ramp north-dipping structure that steepens as it approaches the surface (orange line in Fig. S7). The absence of the broader long-wavelength signal, ∼10 km north of the high-velocity gradient at the southern topography front, in the Sentinel-1 measurements, suggest that the deformation is essentially concentrated at shallower depth during 2014 to 2019. Horizontal surface displacements extracted from the 2014-2019 period across the Delingha anticline (blue profile in Fig. 4c) are in agreement with movement of the hanging wall towards the south and with a shallow north-dipping thrust fault with steep horizontal gradient localised on the tip of the dislocation (Fig. S8). However, an additional localised extension on the southern limb of the anticline is also measured. This observation might be the effect of the buckling of the crest, which collapses the southern limb and results in relative shortening across the blind north-dipping fault that is larger than the overall shortening over the region (Fig. 4c). In addition, contrary to what is expected from an elastic dislocation, no subsidence is observed north and south of the hanging wall (red profile in Fig. 4c, Fig. S8). Vertical velocity profiles show an asymmetric uplift, with steep velocity gradients in the southern limbs, which coincides with the region with high horizontal motion to the south, a maximum of uplift at the front of the crest, and a gently vertical gradient on the northern dipping limb. Kinematic fault-bend fold models predict that, slip on the dipping ramp produces uplift of the back-limb above the ramp alone, whereas fault-

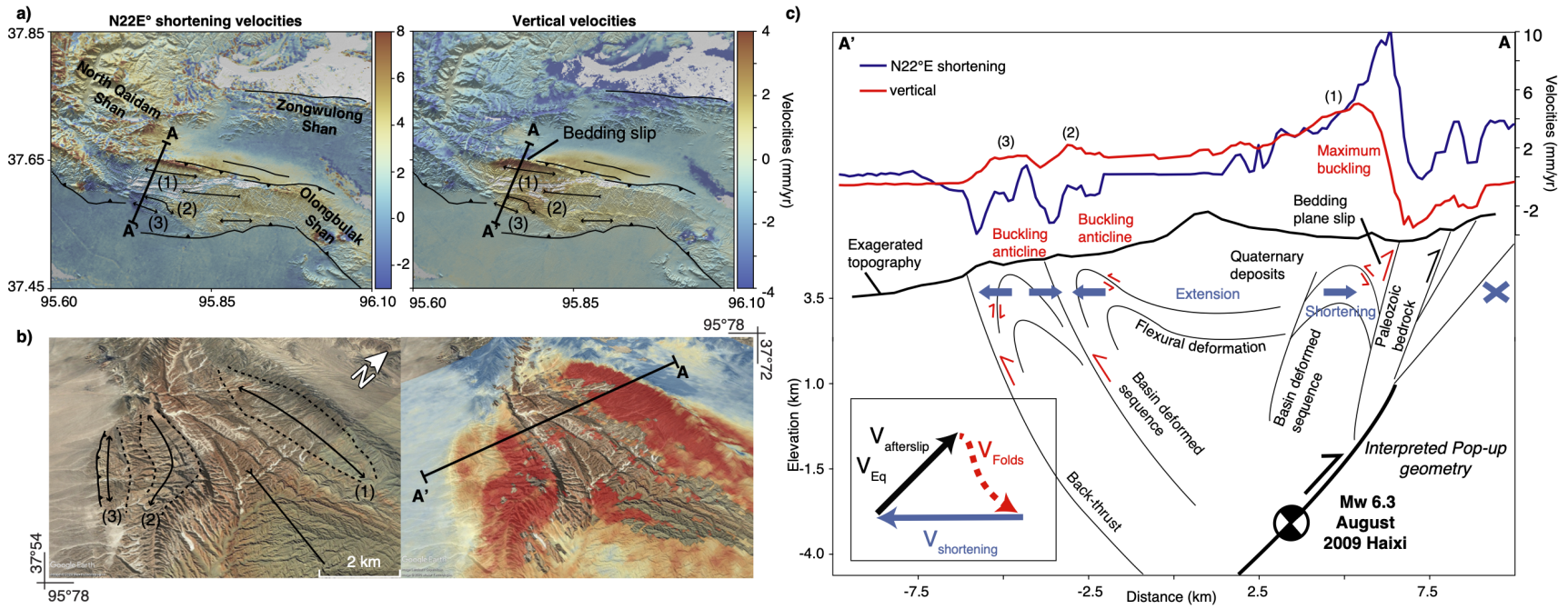

Figure 5. a) N22E shortening and vertical decomposition of the velocity of the Haixi earthquakes area in Fig. 3 obtained from Sentinel-1 post-seismic LOS velocities for ascending track 172 and descending track 004. Figure extend is as Fig. 3. b) Google-Earth imagery with interpreted geomorphological structures side-by-side with the enlargement of the vertical velocities of (a). Mapped active thrust faults are denoted by solid triangles in the hanging wall. The axes (black lines) and limbs (dashed lines) of the three anticlines are inferred from the geomorphology. c) Topography (black lines) and surface velocity profiles (N22°E shortening in blue, vertical in red) with interpreted structural cross-section sketches. We infer complex imbricated folds that underlain the Olongbulak pop-up structure. Inserts at the bottom left show interpreted conceptual conservation of motion vectors across the fault-system, where the faults and associated folds move at different periods of the seismic cycle.

propagation and detachment fold model uplift the crest (Suppe, 1983; Brandes & Tanner, 2014). We propose that the measured vertical velocity with Sentinel-1 data corresponds to the long-term uplift of the fold, which is here consistent with a fold underlain by a north-dipping thrust fault (Suppe, 1983; Walker, 2006; Brandes & Tanner, 2014; Daëron et al., 2007), with a steep but eroded forelimb and a more gently dipping backlimb, as conceptually proposed in Fig. 4c. The findings suggest that the 2003 coseismic rupture in the basement induced aseismic fault slip in the sedimentary cover, which has evolved from localised slip shortly after the event (during the 2003-2009 period, approximatively) to a more distributed deformation (during the 2014-2019 period, approximatively) across the anticline. This transient strain release is still ongoing in 2019, more than 16 years after the earthquake.

From our InSAR measurements and the structural cross-section of Yin, Dang, Wang, et al. (2008), Guihua et al. (2013) and Daout, Steinberg, et al. (2020), we infer for the Olongbulak pop-up, the structural cross-section of Fig. 5c. From the inverted shortening rates (Fig. 5a), the Olongbulak Shan is mainly moving to the north, with a concentration of the shortening gradient on the northwestern part of the range. However, a movement in the SW direction is also observed on the southwestern part of the system, highlighting the activity of the north-dipping branches, in the southern side of the Olongbulak range and some extension between the northern and southern side of the pop-up structure. Curiously, the shortening across the whole structure is close to zero (Fig. 5c), which may indicate a motion driven from below with the vertical motion. From 2014 to 2019, vertical ground motion is observed across the whole $\sim$10 km-large structure with three maxima that coincided with the three inferred anticlines, numbered (1), (2) and (3) in Fig. 5b, from our own geomorphological analysis and bibliographic reviews (Yin, Dang, Wang, et al., 2008; Elliott et al., 2011; Guihua et al., 2013). Differences between ascending track 099 and descending track 004, due to the N22°E shortening (Fig. 3a), are mainly observed in the northern part of the pop-up structure, where the LOS surface velocity is also sharp and asymmetric. Surface velocities there may be compatible with shallow aseismic slip on a south-dipping fault (Fig. S8), located on the upward prolongation of the south-dipping and shallow 2009 rupture (Fig. 5c). However, higher rates of surface velocities are located between the basin deformed sedimentary sequences of the Olongbulak range and the Paleozoic bedrock, north of it (Fig. 5b). As we did not identify fault traces or folds in the satellite imagery where the maximum uplift is measured and as two different rock types are identified from the satellite imagery and from the geological mapping of Yin, Dang, Wang, et al. (2008), we interpret the high surface displacements here as due to bedding planes slip along the stratigraphic contacts between a major anticline to the south (marked 1) and the Paleozoic strata to the north. In this

complex structure, with imbricated Cenozoic and Mesozoic strata and multiple folds of different ages, old bedding planes might have been reactivated as faults following more recent events, such as the 2009 south-dipping Haixi earthquake (Fig. 5c).

In the southern part of the Olongbulak Shan, two secondary uplift lobes are colocated with the two identified southern anticlines, marked (2) and (3) (Fig. 5a); small symmetric localised N22°E horizontal components are also observed there. The two folds show truncated geological units with sharp contacts on the southern sides between the uplifted rocks and the more recent deposits on the footwall (Fig. 5b). Those two surface expressions are in agreement with two folds associated with shallow north-dipping faults. The exhumed soft sediments in the core of the two anticlines (black lines in Fig. 5b) are light-coloured in comparison to the harder and more resistant rocks exposed on the two limbs of the folds (black dashed-lines in Fig. 5b). Because of differential erosion, the back-limbs look steeper in comparison to the crest and the forelimbs (Fig. 5b). Because the surface displacements coincide with the two fold morphologies and because the symetric shortening signal is not in agreement with what would be expected from slip on thrust faults, we interpret the signal not as the direct result of elastic slip along a north-dipping thrust structure, but as distributed fold-growth deformation of the upper layers induced by slip during the 2008-2009 Haixi events and afterslip folowing them. The deformation might be accommodated by multiple mechanisms such as off-fault deformation along bedding planes or ductile flexural shear creating mainly vertical uplift in combination with internal shearing with no net shortening across the whole structure. To conclude, the dip-angle between the main south-dipping thrust underlying the Olongbulak pop-up that ruptured during the 2009 Haixi earthquake (conceptual back arrow in Fig. 5c, insert) and the horizontal shortening (conceptual blue arrow in Fig. 5c, insert) creates a reverse north-dipping component of motion that must be accommodated during the seismic cycle either by seismic or aseismic deformation (red arrow in Fig. 5c, insert). The measurements suggest that this vertical partitioning is, at least in part, compensated by aseismic post-seismic folding across the whole structure and localised along the anticlines observed in the geomorphology.

4.2 Aseismic transient phenomena

Since the discovery at different crustal depths of aseismic transient phenomena from observations made using geodetic networks, large efforts have been made by the geodetic and earthquake communities to better understand and localise these events occurring at low rupture speed and to improve the understanding of their interaction with earthquakes (e.g., Obara & Hirose, 2006; Collettini et al., 2011; Rousset et al., 2016; Hawthorne

et al., 2016; Socquet et al., 2017; Behr & Bürgmann, 2020). The findings of this study illustrate that moderate earthquakes can trigger anelastic transient responses of the shallow crust after several decades after it. It shows that ductile deformation can be produced in low strain regimes by moderate stress changes and at shallow depths. These observations may support thick fault models, documented both at shallow and greater depths, where velocity-strengthening frictional behaviour is enhanced by the presence of weak materials, such as phyllosilicate-rich sediments, within heterogeneous fault zones. In those models, weak rocks surround mafic and more competent materials, and accommodate the transient deformation by pressure solution, foliation-parallel sliding, and microfolds (e.g., Niemeijer & Spiers, 2005; Collettini et al., 2011; Lavier et al., 2013; Reber et al., 2014). This study demonstrates that transient aseismic events, detected both at shallow and greater depths during the inter- or post-seismic periods, might not be always linked with slip on a thin main fault or slab. On the contrary, they might also be associated with ductile and plastic deformation processes, either triggered by an earthquake on the main adjacent fault-segment (post-seismic transients), or by a transient increases in stress concentrations within the more competent rocks of a thick and heterogeneous shear zone (slow-slip transients).

5 Conclusion

The improved spatial and temporal sampling offered by the new generation of Sentinel-1 radar data in both ascending and descending geometries, has enabled to resolve the vertical and shortening component across two fold-and-thrust belts in the Qaidam Basin, in China. The study reveals a link between the post-seismic phase and the long-term geomorphology of the tectonic structures. We interpret the non-logarithmic long-term ground aseismic surface displacements observed up to 16 years after the seismic events as off-fault volumetric deformation associated with active folding. In the two examples, co-seismic slip is translated into permanent deformation during the post-seismic phase through signals that match young anticlines observed in the morphology, and that cannot be simply explained by elastic slip along dislocations. The results demonstrate, along with other observations and models (e.g., Ainscoe et al., 2017; Bonanno et al., 2017; Johnson, 2018), that it not always valid to assume that fold growth above blind reverse faults is co-seismic or that it is appropriate to model it by slip on a fault, because a significant part of the finite shortening may occur as distributed off-fault deformation (flexural slip, interbed flow, shearing) during the post-seismic or inter-seismic phases. The study highlights that the contribution of distributed deformation and slip-partitioning between secondary structures needs to be considered in earthquake cycle models, analyses of fault-related folds and the assessments of earthquake hazard from surface measurements.

Acknowledgments

The Envisat SAR data are provided by the European Space Agency (ESA) and can be acquired through an online proposal (https://earth.esa.int/web/guest/missions/esa-operational-eo-missions/envisat). Sentinel-1 data are freely available online at https://scihub.copernicus.eu. Topographic data are provided by NASA and available also online at https://e4ftl01.cr.usgs.gov/. This research was supported by the Natural Environment Research Council through the Looking into the Continents from Space (LiCS) large grant (NE/K011006/1) and the Centre for the Observation and modeling of Earthquakes, Volcanoes and Tectonics (COMET).

References

Ainscoe, E., Elliott, J., Copley, A., Craig, T., Li, T., Parsons, B., & Walker, R. (2017). Blind thrusting, surface folding, and the development of geological structure in the Mw 6.3 2015 Pishan (China) earthquake. *Journal of Geophysical Research: Solid Earth*, *122*(11), 9359–9382.

Ansari, H., De Zan, F., & Parizzi, A. (2020). Study of systematic bias in measuring surface deformation with SAR Interferometry. *IEEE*.

Barnhart, W. D., Brengman, C. M., Li, S., & Peterson, K. E. (2018). Ramp-flat basement structures of the Zagros Mountains inferred from co-seismic slip and afterslip of the 2017 Mw 7.3 Darbandikhan, Iran/Iraq earthquake. *Earth and Planetary Science Letters*, *496*, 96–107.

Barnhart, W. D., Lohman, R. B., & Mellors, R. J. (2013). Active accommodation of plate convergence in Southern Iran: Earthquake locations, triggered aseismic slip, and regional strain rates. *Journal of Geophysical Research: Solid Earth*, *118*(10), 5699–5711.

Behr, W., & Bürgmann, R. (2020). What's down there? the structures, materials and environment of deep-seated tremor and slip. *Phil. Trans. R. Soc.*.

Belabbès, S., Meghraoui, M., Çakir, Z., & Bouhadad, Y. (2009). InSAR analysis of a blind thrust rupture and related active folding: the 1999 Ain Temouchent earthquake (Mw 5.7, Algeria) case study. *Journal of Seismology*, *13*(4), 421–432.

Bibi, S., Wang, L., Li, X., Zhou, J., Chen, D., & Yao, T. (2018). Climatic and associated cryospheric, biospheric, and hydrological changes on the Tibetan Plateau: a review. *International Journal of Climatology*, *38*, e1–e17.

Bonanno, E., Bonini, L., Basili, R., Toscani, G., & Seno, S. (2017). How do horizontal, frictional discontinuities affect reverse fault-propagation folding? *Journal of Structural Geology*, *102*, 147–167.

Brandes, C., & Tanner, D. C. (2014). Fault-related folding: A review of kinematic

models and their application. *Earth-Science Reviews*, *138*, 352–370.

Collettini, C., Niemeijer, A., Viti, C., Smith, S. A., & Marone, C. (2011). Fault structure, frictional properties and mixed-mode fault slip behavior. *Earth and Planetary Science Letters*, *311*(3-4), 316–327.

Copley, A. (2014). Postseismic afterslip 30 years after the 1978 Tabas-e-Golshan (Iran) earthquake: observations and implications for the geological evolution of thrust belts. *Geophysical Journal International*, *197*(2), 665–679.

Daëron, M., Avouac, J.-P., & Charreau, J. (2007). Modeling the shortening history of a fault tip fold using structural and geomorphic records of deformation. *Journal of Geophysical Research: Solid Earth*, *112*(B3).

Daout, S., Barbot, S., Peltzer, G., Doin, M.-P., Liu, Z., & Jolivet, R. (2016). Constraining the kinematics of metropolitan Los Angeles faults with a slip-partitioning model. *Geophys. Res. Lett.*.

Daout, S., Dini, B., Haeberli, W., Doin, M.-P., & Parsons, B. (2020). Ice loss in the Northeastern Tibetan Plateau permafrost as seen by 16 yr of ESA SAR missions. *Earth and Planetary Science Letters*, *545*, 116404.

Daout, S., Doin, M.-p., Peltzer, G., Lasserre, C., Socquet, A., Volat, M., & Sudhaus, H. (2018). Strain Partitioning and Present-Day Fault Kinematics in NW Tibet From Envisat SAR Interferometry. *Journal of Geophysical Research: Solid Earth*, *123*(3), 2462–2483. doi: 10.1002/2017JB015020

Daout, S., Steinberg, A., Isken, M. P., Heimann, S., & Sudhaus, H. (2020). Illuminating the Spatio-Temporal Evolution of the 2008–2009 Qaidam Earthquake Sequence with the Joint Use of InSAR Time Series and Teleseismic Data. *Remote Sensing*, *12*(17), 2850.

Daout, S., Sudhaus, H., Kausch, T., Steinberg, A., & Dini, B. (2019). Interseismic and postseismic shallow creep of the North Qaidam Thrust faults detected with a multitemporal InSAR analysis. *Journal of Geophysical Research: Solid Earth*, *124*(7), 7259–7279.

Davis, D., Suppe, J., & Dahlen, F. (1983). Mechanics of fold-and-thrust belts and accretionary wedges. *Journal of Geophysical Research: Solid Earth*, *88*(B2), 1153–1172.

Doin, M.-P., Lasserre, C., Peltzer, G., Cavalié, O., & Doubre, C. (2009). Corrections of stratified tropospheric delays in SAR interferometriy: Validation with global atmospheric models. *J. Applied Geophysics*, *69*, 35-50.

Doin, M.-P., Lodge, F., Guillaso, S., Jolvet, R., Lasserre, C., Ducret, G., ... Pinel, V. (2011). Presentation of the small baseline NSBAS Processing chain on a case example : The Etna deformation monitoring from 2003 to 2010 using

Envisat data. *Proc. esaFringe*.

Doin, M.-P., Twardzik, C., Ducret, G., Lasserre, C., Guillaso, S., & Jianbao, S. (2015). InSAR measurement of the deformation around Siling Co Lake: Inferences on the lower crust viscosity in central Tibet. *J. Geophys. Res.: Solid Earth*, *120*(7), 5290–5310.

Dolan, J. F., & Avouac, J.-P. (2007). Introduction to special section: Active fault-related folding: Structural evolution, geomorphologic expression, paleoseismology, and seismic hazards. *Journal of Geophysical Research: Solid Earth*, *112*(B3).

Elliott, J., Bergman, E., Copley, A., Ghods, A., Nissen, E., Oveisi, B., ... Yamini-Fard, F. (2015). The 2013 mw 6.2 Khaki-Shonbe (Iran) earthquake: Insights into seismic and aseismic shortening of the Zagros sedimentary cover. *Earth and Space Science*, *2*(11), 435–471.

Elliott, J., Jolivet, R., González, P., Avouac, J.-P., Hollingsworth, J., Searle, M., & Stevens, V. (2016). Himalayan megathrust geometry and relation to topography revealed by the Gorkha earthquake. *Nature Geoscience*, *9*(2), 174–180.

Elliott, J., Parsons, B., Jackson, J., Shan, X., Sloan, R., & Walker, R. (2011). Depth segmentation of the seismogenic continental crust: The 2008 and 2009 Qaidam earthquakes. *Geophysical research letters*, *38*(6).

Fang, X., Zhang, W., Meng, Q., Gao, J., Wang, X., King, J., ... Miao, Y. (2007). High-resolution magnetostratigraphy of the Neogene Huaitoutala section in the eastern Qaidam Basin on the NE Tibetan Plateau, Qinghai Province, China and its implication on tectonic uplift of the NE Tibetan plateau. *Earth and Planetary Science Letters*, *258*(1-2), 293–306.

Feng, W. (2015). *Modelling co-and post-seismic displacements revealed by inSAR, and their implications for fault behaviour* (Unpublished doctoral dissertation). University of Glasgow.

Fielding, E. J., Wright, T. J., Muller, J., Parsons, B. E., & Walker, R. (2004). Aseismic deformation of a fold-and-thrust belt imaged by synthetic aperture radar interferometry near Shahdad, southeast Iran. *Geology*, *32*(7), 577–580.

Gonzalez-Mieres, R., & Suppe, J. (2006). Relief and shortening in detachment folds. *Journal of Structural Geology*, *28*(10), 1785–1807.

Grandin, R. (2015). Interferometric Processing of SLC Sentinel-1 TOPS Data. *Fringe 2015*(731), 36. doi: 10.1109/TGRS.2015.2497902

Grandin, R., Doin, M.-P., Bollinger, L., Pinel-Puysségur, B., Ducret, G., Jolivet, R., & Sapkota, S. N. (2012). Long-term growth of the Himalaya inferred from interseismic InSAR measurement. *Geology*, *40*(12), 1059–1062.

Grandin, R., Klein, E., Métois, M., & Vigny, C. (2016). Three-dimensional displacement field of the 2015 mw8. 3 illapel earthquake (chile) from across-and along-track sentinel-1 tops interferometry. *Geophysical Research Letters*, *43*(6), 2552–2561.

Guihua, C., Xiwei, X., Ailan, Z., Xiaoqing, Z., Renmao, Y., Klinger, Y., & Nocquet, J.-M. (2013). Seismotectonics of the 2008 and 2009 Qaidam earthquakes and its implication for regional tectonics. *Acta Geologica Sinica-English Edition*, *87*(2), 618–628.

Guilbaud, C., Simoes, M., Barrier, L., Laborde, A., Van der Woerd, J., Li, H., ... Murray, A. (2017). Kinematics of active deformation across the western kunlun mountain range (Xinjiang, China) and potential seismic hazards within the southern Tarim Basin. *Journal of Geophysical Research: Solid Earth*, *122*(12), 10–398.

Hawthorne, J. C., Bostock, M. G., Royer, A. A., & Thomas, A. M. (2016). Variations in slow slip moment rate associated with rapid tremor reversals in Cascadia. *Geochemistry, Geophysics, Geosystems*, *17*(12), 4899–4919.

Huang, W.-J., & Johnson, K. M. (2016). A fault-cored anticline boundary element model incorporating the combined fault slip and buckling mechanisms. *Terrestrial, Atmospheric & Oceanic Sciences*, *27*(1).

Johnson, K. M. (2018). Growth of fault-cored anticlines by flexural slip folding: Analysis by boundary element modeling. *Journal of Geophysical Research: Solid Earth*, *123*(3), 2426–2447.

Jolivet, R., Grandin, R., Lasserre, C., Doin, M.-P., & Peltzer, G. (2011). Systematic InSAR tropospheric phase delay corrections from global meteorological reanalysis data. *Geophys. Res. Lett.*, *38*(17).

Lavier, L. L., Bennett, R. A., & Duddu, R. (2013). Creep events at the brittle ductile transition. *Geochemistry, Geophysics, Geosystems*, *14*(9), 3334–3351.

Liang, S., Gan, W., Shen, C., Xiao, G., Liu, J., Chen, W., ... Zhou, D. (2013, October). Three-dimensional velocity field of present-day crustal motion of the Tibetan Plateau derived from GPS measurements. *J. Geophys. Res.*, *118*(10), 5722–5732.

Liu, Y., Xu, C., Li, Z., Wen, Y., Chen, J., & Li, Z. (2016). Time-dependent afterslip of the 2009 mw 6.3 dachaidan earthquake (china) and viscosity beneath the qaidam basin inferred from postseismic deformation observations. *Remote Sensing*, *8*(8), 649.

Liu, Y., Xu, C., Wen, Y., & Fok, H. S. (2015). A new perspective on fault geometry and slip distribution of the 2009 Dachaidan Mw 6.3 earthquake from InSAR

observations. *Sensors*, *15*(7), 16786–16803.

Liu, Y., Xu, C., Wen, Y., & Li, Z. (2016). Post-seismic deformation from the 2009 mw 6.3 dachaidan earthquake in the northern qaidam basin detected by small baseline subset insar technique. *Sensors*, *16*(2), 206.

López-Quiroz, P., Doin, M.-P., Tupin, F., Briole, P., & Nicolas, J.-M. (2009). Time series analysis of Mexico City subsidence constrained by radar interferometry. *J. Applied Geophysics*, *69*(1), 1–15.

Mackenzie, D., Elliott, J., Altunel, E., Walker, R., Kurban, Y., Schwenninger, J.-L., & Parsons, B. (2016). Seismotectonics and rupture process of the Mw 7.1 2011 Van reverse-faulting earthquake, eastern Turkey, and implications for hazard in regions of distributed shortening. *Geophysical Journal International*, *206*(1), 501–524.

Mariniere, J., Nocquet, J., Beauval, C., Champenois, J., Audin, L., Alvarado, A., ... Socquet, A. (2020). Geodetic evidence for shallow creep along the Quito fault, Ecuador. *Geophysical Journal International*, *220*(3), 2039–2055.

Medwedeff, D. A., & Suppe, J. (1997). Multibend fault-bend folding. *Journal of Structural Geology*, *19*(3-4), 279–292.

Métois, M., Benjelloun, M., Lasserre, C., Grandin, R., Barrier, L., Dushi, E., & Koçi, R. (2020). Subsidence associated with oil extraction, measured from time series analysis of sentinel-1 data: case study of the patos-marinza oil field, albania. *Solid Earth*, *11*(2).

Meyer, B., Tapponnier, P., Bourjot, L., Metivier, F., Gaudemer, Y., Peltzer, G., ... Zhitai, C. (1998). Crustal thickening in Gausu-Qinghai, lithospheric mantle subduction, and oblique, strike-slip controlled growth of the Tibet Plateau. *Geophy. J. Int.*, *135*.

Niemeijer, A. R., & Spiers, C. J. (2005). Influence of phyllosilicates on fault strength in the brittle-ductile transition: Insights from rock analogue experiments. *Geological Society, London, Special Publications*, *245*(1), 303–327.

Nissen, E., Ghorashi, M., Jackson, J., Parsons, B., & Talebian, M. (2007). The 2005 Qeshm island earthquake (Iran). a link between buried reverse faulting and surface folding in the Zagros simply folded belt? *Geophysical Journal International*, *171*(1), 326–338.

Obara, K., & Hirose, H. (2006). Non-volcanic deep low-frequency tremors accompanying slow slips in the southwest Japan subduction zone. *Tectonophysics*, *417*(1-2), 33–51. doi: 10.1016/j.tecto.2005.04.013

Pang, J., Yu, J., Zheng, D., Wang, W., Ma, Y., Wang, Y., ... Wang, Y. (2019). Neogene expansion of the qilian shan, north tibet: Implications for the dy-

namic evolution of the tibetan plateau. *Tectonics*, *38*(3), 1018–1032.

Reber, J. E., Hayman, N. W., & Lavier, L. L. (2014). Stick-slip and creep behavior in lubricated granular material: Insights into the brittle-ductile transition. *Geophysical Research Letters*, *41*(10), 3471–3477.

Rosen, P. A., Hensley, S., Peltzer, G., & Simons, M. (2004). Updated repeat orbit interferometry package released. *Eos, Transactions American Geophysical Union*, *85*(5), 47–47.

Rousset, B., Jolivet, R., Simons, M., Lasserre, C., Riel, B., Milillo, P., ... Renard, F. (2016). An aseismic slip transient on the North Anatolian Fault. *Geophys. Res. Lett.*, *43*(7), 3254–3262.

Sathiakumar, S., Barbot, S., & Hubbard, J. (2020). Earthquake cycles in fault-bend folds. *Journal of Geophysical Research: Solid Earth*, e2019JB018557.

Shaw, J. H., Connors, C. D., Suppe, J., et al. (2005). *Seismic interpretation of contractional fault-related folds: An aapg seismic atlas* (Vol. 53). American Association of Petroleum Geologists Tulsa.

Shaw, J. H., Plesch, A., Dolan, J. F., Pratt, T. L., & Fiore, P. (2002). Puente hills blind-thrust system, Los Angeles, California. *Bulletin of the Seismological Society of America*, *92*(8), 2946–2960.

Socquet, A., Valdes, J. P., Jara, J., Cotton, F., Walpersdorf, A., Cotte, N., ... Norabuena, E. (2017). An 8 month slow slip event triggers progressive nucleation of the 2014 Chile megathrust. *Geophysical Research Letters*, *44*(9), 4046–4053.

Stein, R. S., & King, G. C. (1984). Seismic potential revealed by surface folding: 1983 Coalinga, California, earthquake. *Science*, *224*(4651), 869–872.

Sun, C.-H., Xu, F., Yang, Y.-B., Qian, R.-Y., & Meng, X.-H. (2012). Focal mechanism solutions of the 2003 Delingha, Qinghai M6.7 earthquake sequence and their tectonic implications. *Chinese Journal of Geophysics*, *55*(6), 680–688.

Suppe, J. (1983). Geometry and kinematics of fault-bend folding. *American Journal of science*, *283*(7), 684–721.

Suppe, J., & Medwedeff, D. A. (1990). Geometry and kinematics of fault-propagation folding. *Eclogae Geologicae Helvetiae*, *83*(3), 409–454.

Tapponnier, P., Meyer, B., Avouac, J. P., Peltzer, G., Gaudemer, Y., Shunmin, G., ... others (1990). Active thrusting and folding in the Qilian Shan, and decoupling between upper crust and mantle in northeastern Tibet. *Earth and Planetary Science Letters*, *97*(3-4), 382–403.

Tapponnier, P., Zhiqin, X., Roger, F., Meyer, B., Arnaud, N., Wittlinger, G., & Jingsui, Y. (2001, November). Oblique stepwise rise and growth of the Tibet

Plateau. *Science*, *294*(5547), 1671-1677.

Tizzani, P., Castaldo, R., Solaro, G., Pepe, S., Bonano, M., Casu, F., ... others (2013). New insights into the 2012 Emilia (Italy) seismic sequence through advanced numerical modeling of ground deformation InSAR measurements. *Geophysical research letters*, *40*(10), 1971–1977.

Veloza, G., Taylor, M., Mora, A., & Gosse, J. (2015). Active mountain building along the eastern Colombian Subandes: A folding history from deformed terraces across the Tame anticline, Llanos Basin. *Bulletin*, *127*(9-10), 1155–1173.

Walker, R. T. (2006). A remote sensing study of active folding and faulting in southern Kerman province, SE Iran. *Journal of Structural Geology*, *28*(4), 654–668.

Wang, W., Qiao, X., Yang, S., & Wang, D. (2017). Present-day velocity field and block kinematics of Tibetan Plateau from GPS measurements. *Geophys.J. Int.*, *208*(2), 1088–1102.

Ward, S. N., & Valensise, G. (1994). The Palos Verdes terraces, California: Bathtub rings from a buried reverse fault. *Journal of Geophysical Research: Solid Earth*, *99*(B3), 4485–4494.

Whipple, K. X., Shirzaei, M., Hodges, K. V., & Arrowsmith, J. R. (2016). Active shortening within the Himalayan orogenic wedge implied by the 2015 Gorkha earthquake. *Nature Geoscience*, *9*(9), 711–716.

Wimpenny, S., Copley, A., & Ingleby, T. (2017). Fault mechanics and post-seismic deformation at Bam, SE Iran. *Geophysical Journal International*, *209*(2), 1018–1035.

Wright, T. J., Parsons, B. E., & Lu, Z. (2004). Toward mapping surface deformation in three dimensions using InSAR. *Geophysical Research Letters*, *31*(1).

Yin, A., Dang, Y.-Q., Wang, L.-C., Jiang, W.-M., Zhou, S.-P., Chen, X.-H., ... McRivette, M. W. (2008). Cenozoic tectonic evolution of Qaidam Basin and its surrounding regions (part 1): The southern Qilian Shan-Nan shan thrust belt and northern Qaidam Basin. *Geological Society of America Bulletin*, *120*(7-8), 813–846.

Yin, A., Dang, Y.-Q., Zhang, M., Chen, X.-H., & McRivette, M. W. (2008). Cenozoic tectonic evolution of the Qaidam Basin and its surrounding regions (part 3): Structural geology, sedimentation, and regional tectonic reconstruction. *Geological Society of America Bulletin*, *120*(7-8), 847–876.

Yonkee, A., & Weil, A. B. (2010). Reconstructing the kinematic evolution of curved mountain belts: Internal strain patterns in the Wyoming salient, Sevier thrust belt, USA. *GSA Bulletin*, *122*(1-2), 24–49.

Zhou, Y., Thomas, M. Y., Parsons, B., & Walker, R. T. (2018). Time-dependent

postseismic slip following the 1978 Mw 7.3 Tabas-e-Golshan, Iran earthquake revealed by over 20 years of ESA InSAR observations. *Earth and Planetary Science Letters*, *483*, 64–75.

Figure 1.

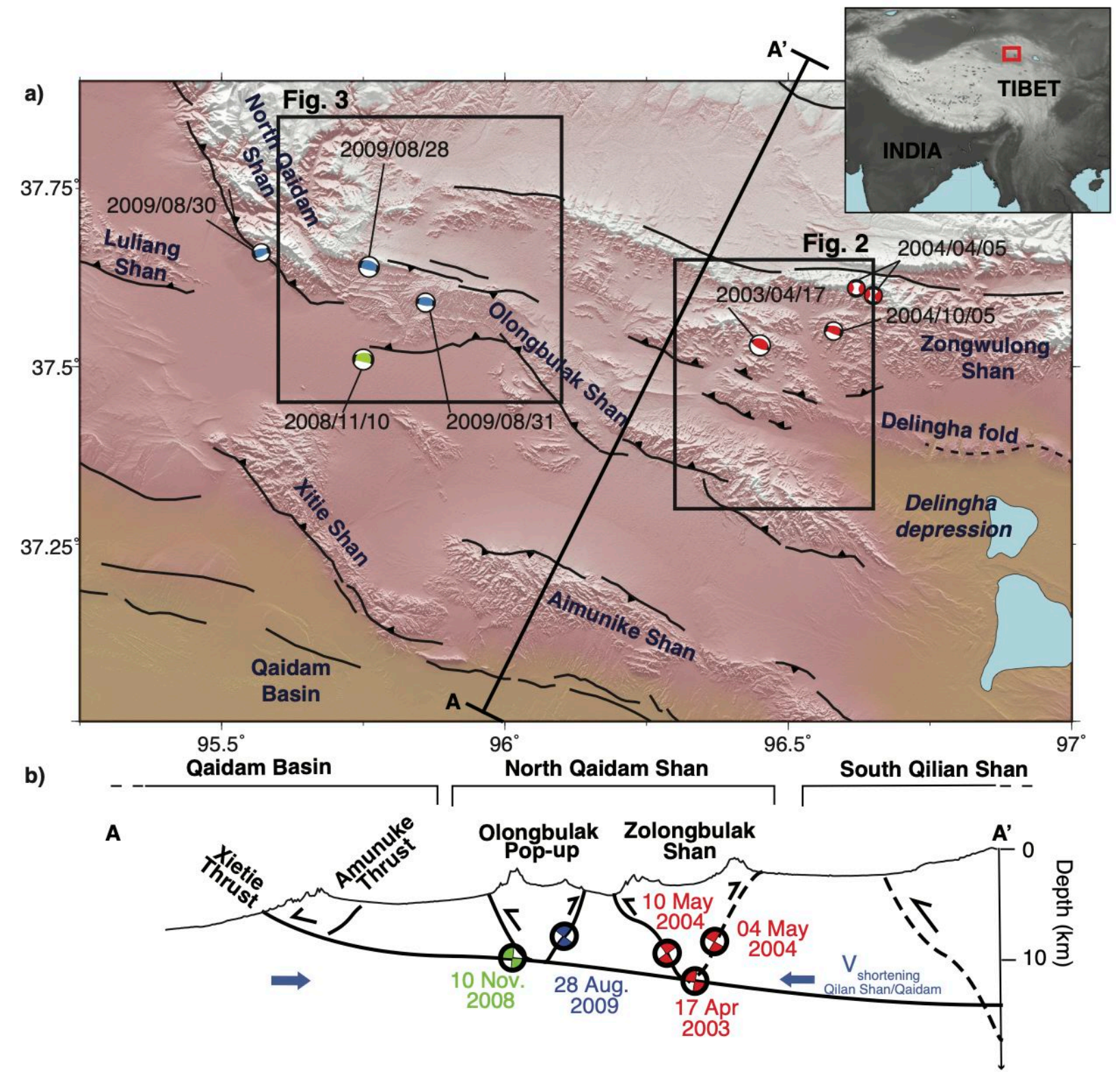
a)
Fig. 3
Fig. 2
A'
A
TIBET
INDIA
North Qaidam Shan
Luliang Shan
Olongbulak Shan
Zongwulong Shan
Delingha fold
Delingha depression
Xitie Shan
Aimunike Shan
Qaidam Basin
2009/08/28
2009/08/30
2008/11/10
2009/08/31
2004/04/05
2003/04/17
2004/10/05
37.75°
37.5°
37.25°
95.5°
96°
96.5°
97°
b)
Qaidam Basin
North Qaidam Shan
South Qilian Shan
A
A'
Xietie Thrust
Amunuke Thrust
Olongbulak Pop-up
Zolongbulak Shan
10 May 2004
04 May 2004
10 Nov. 2008
28 Aug. 2009
17 Apr 2003
V shortening Qilan Shan/Qaidam
0
10
Depth (km)

Figure 2.

a)

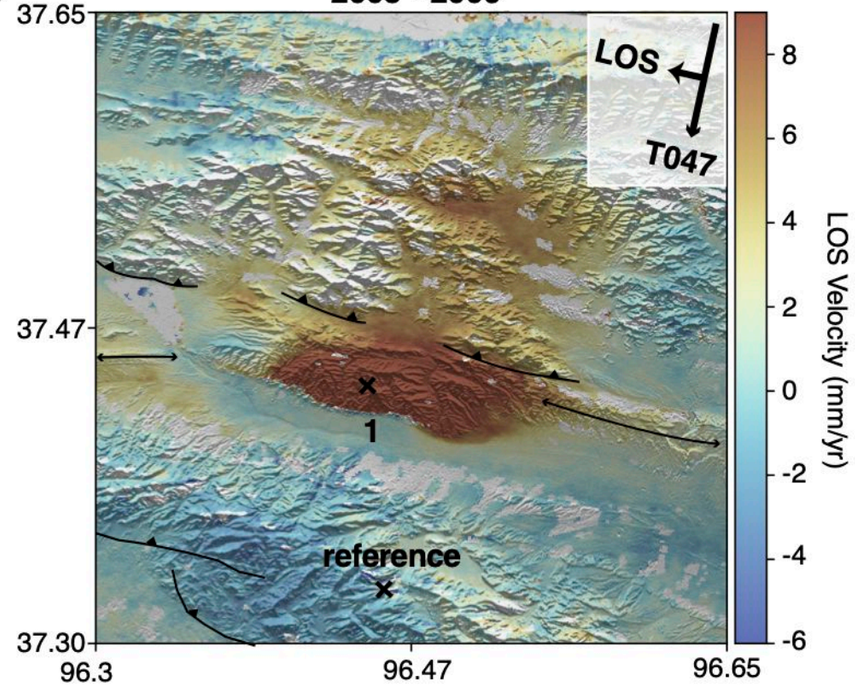
2003 - 2006
LOS
T047
1
reference
37.65
37.47
37.30
96.3
96.47
96.65
LOS Velocity (mm/yr)

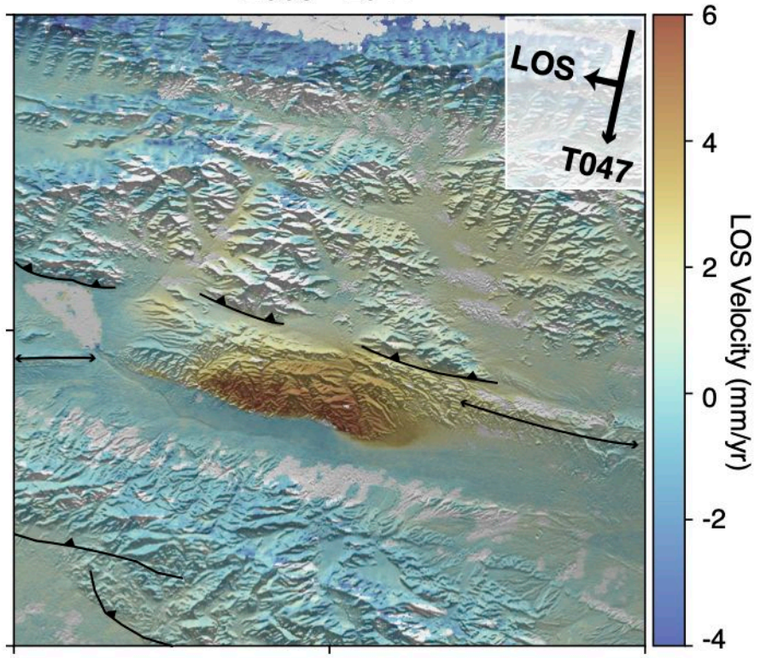
2006 - 2011
LOS
T047
LOS Velocity (mm/yr)

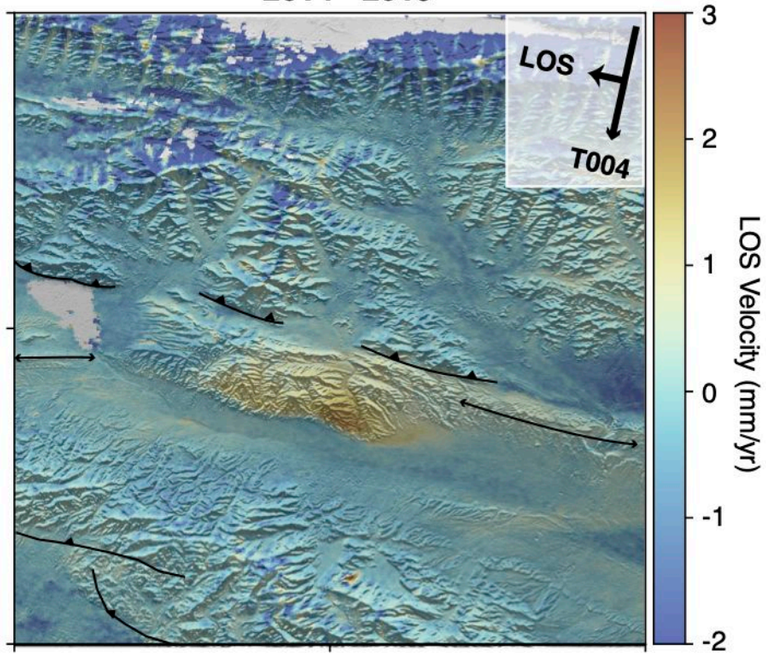
2014 - 2019
LOS
T004
LOS Velocity (mm/yr)

b)

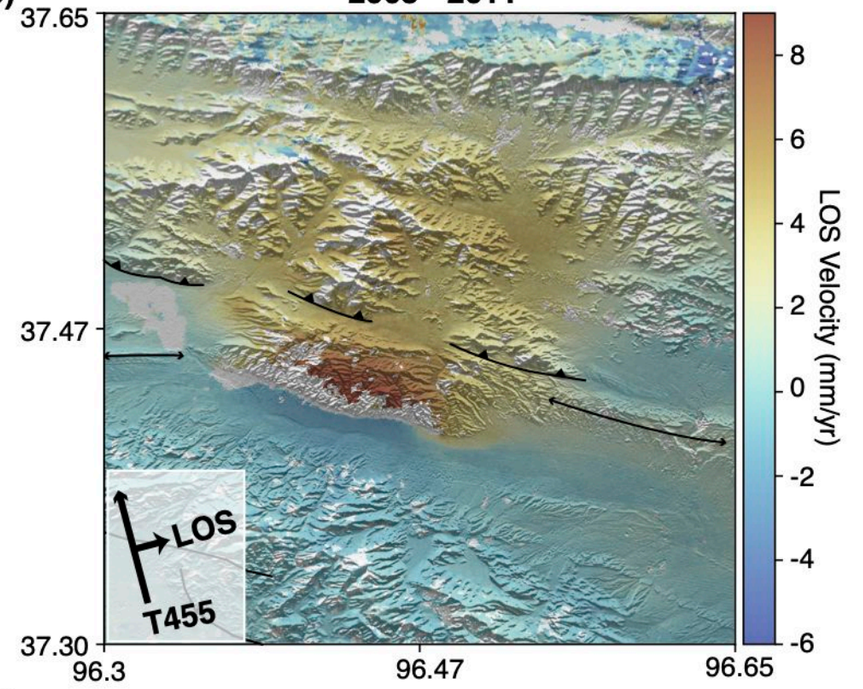
2003 - 2011
LOS
T455
37.65
37.47
37.30
96.3
96.47
96.65
LOS Velocity (mm/yr)

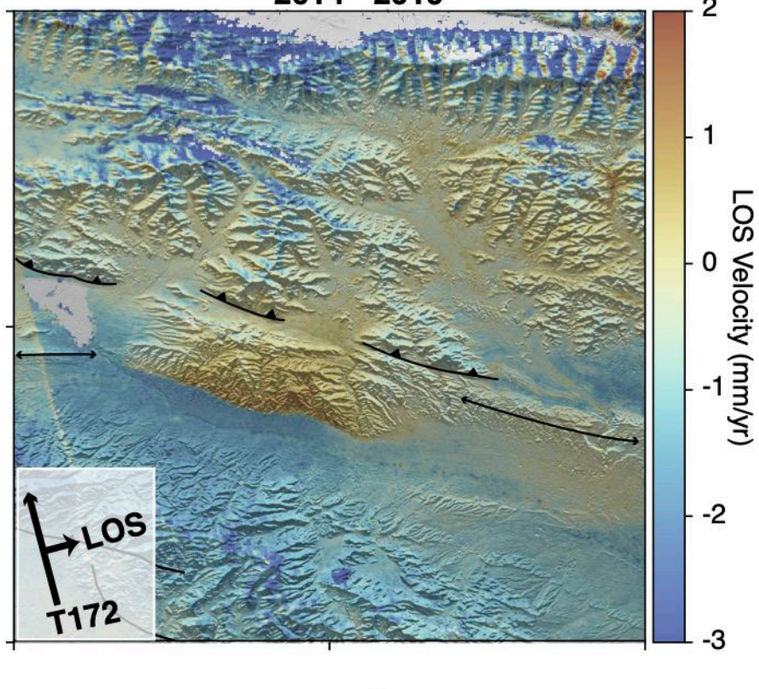
2014 - 2019
LOS
T172
LOS Velocity (mm/yr)

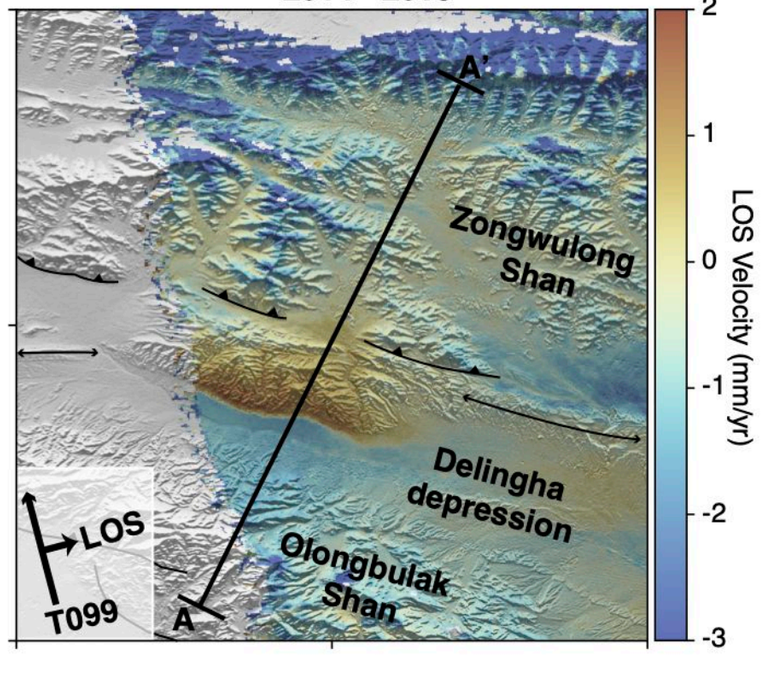
2014 - 2019
A'
A
Zongwulong Shan
Delingha depression
Olongbulak Shan
LOS
T099
LOS Velocity (mm/yr)

c)

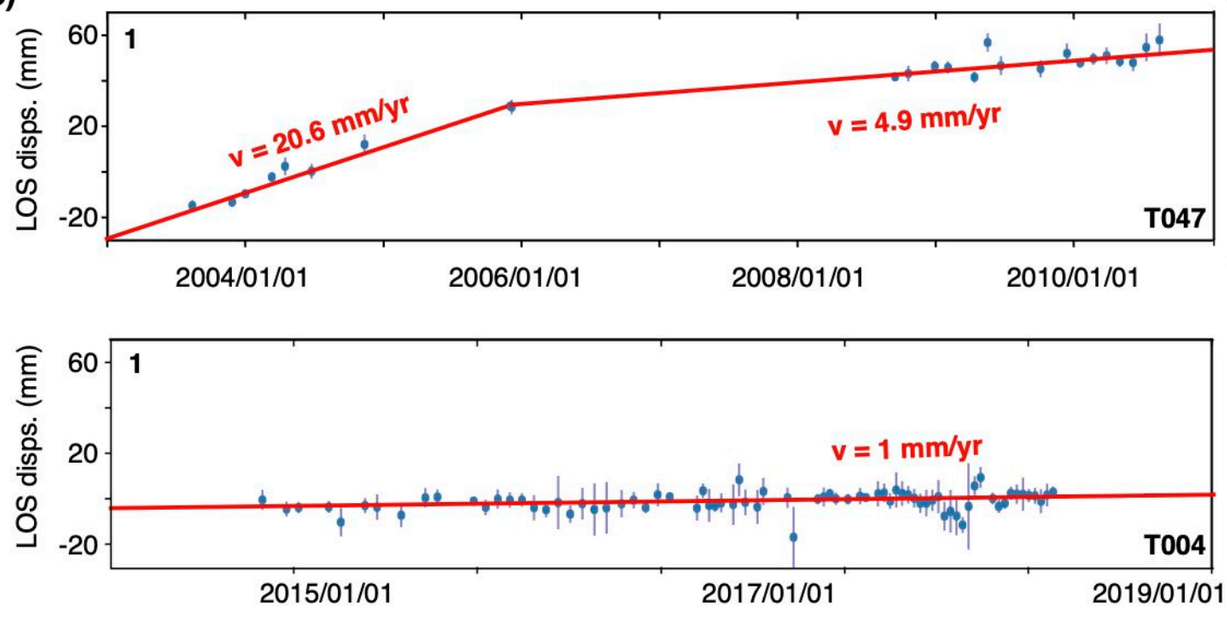
1
v = 20.6 mm/yr
v = 4.9 mm/yr
T047
LOS disps. (mm)
2004/01/01
2006/01/01
2008/01/01
2010/01/01
1
v = 1 mm/yr
T004
2015/01/01
2017/01/01
2019/01/01

d)

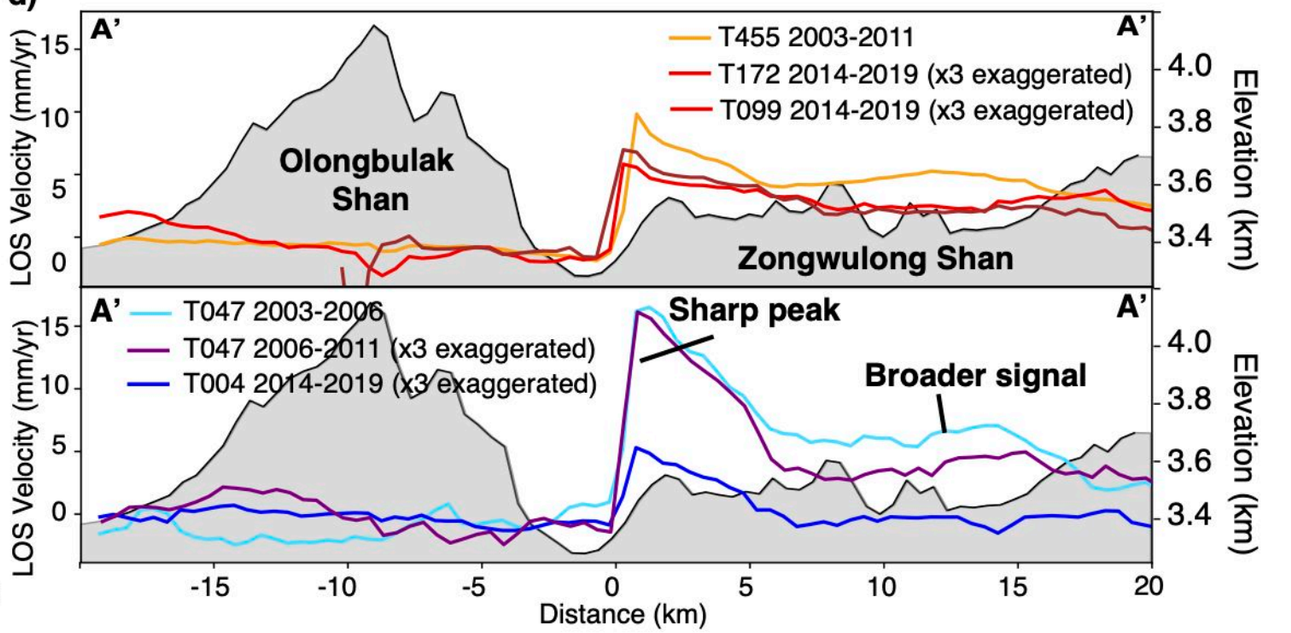
A'
T455 2003-2011
T172 2014-2019 (x3 exaggerated)
T099 2014-2019 (x3 exaggerated)
Olongbulak Shan
Zongwulong Shan
T047 2003-2006
T047 2006-2011 (x3 exaggerated)
T004 2014-2019 (x3 exaggerated)
Sharp peak
Broader signal
LOS Velocity (mm/yr)
Elevation (km)
Distance (km)

Figure 3.

a)

2009-2011

2014-2019

2014-2019

LOS

T319

T004

T172

North Qaidam Shan

Zongwulong Shan

Olongbulak Shan

Bedding plane

Bedrock

Folded sediments

Maximum of deformation

×reference

1

2

A

A'

B

B'

C

C'

37.85

37.65

37.45

95.60

95.85

96.10

LOS Velocity (mm/yr)

30

20

10

0

-10

-20

3

2

1

0

-1

-2

b)

Cumulative LOS displacements (mm)

v = 66 mm/yr

offset = 382 mm

T319

v = 29 mm/yr

offset = 217 mm

T319

v = 3.5 mm/yr

T004

v = 1.9 mm/yr

T004

2009/07/01

2010/01/01

2010/07/01

2011/01/01

2015/01/01

2017/01/01

2019/01/01

c)

T319 2009/09/28 EQ shape (no-units)

T319 2009-2011

T004 2014-2019 (x10 exaggerated)

T172 2014-2019 (x10 exaggerated)

Reak

Secondary uplift

Secondary uplift

Olongbulak Shan

Zongwulong Shan

LOS Velocity (mm/yr)

Elevation (km)

Distance (km)

Figure 4.

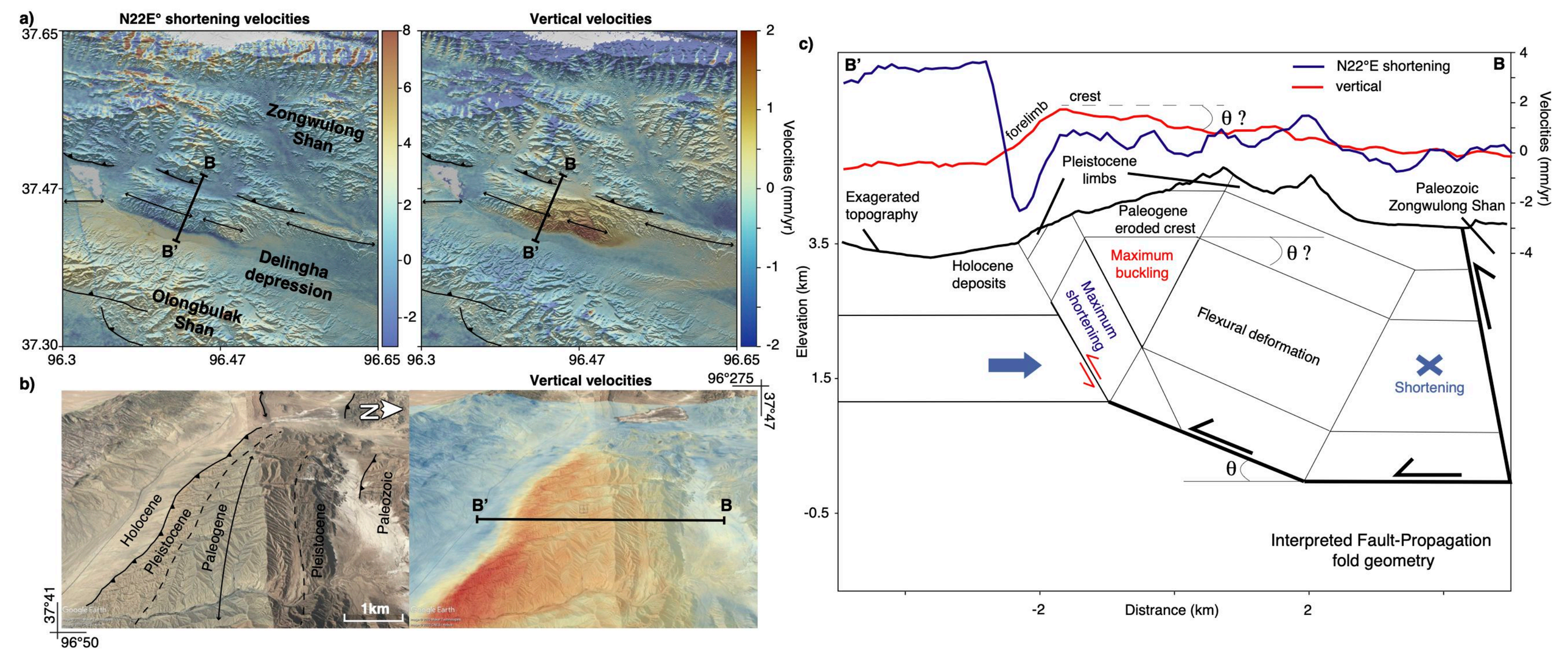
a)
N22E° shortening velocities
Vertical velocities
Zongwulong Shan
Delingha depression
Olongbulak Shan
B
B'
37.65
37.47
37.30
96.3
96.47
96.65
Velocities (mm/yr)
b)
Vertical velocities
96°275
37°47
37°41
96°50
Holocene
Pleistocene
Paleogene
Pleistocene
Paleozoic
1km
Google Earth
c)
B'
B
N22°E shortening
vertical
forelimb
crest
θ ?
Pleistocene limbs
Exagerated topography
Paleogene eroded crest
Paleozoic Zongwulong Shan
Holocene deposits
Maximum buckling
Maximum shortening
Flexural deformation
Shortening
θ
Interpreted Fault-Propagation fold geometry
Elevation (km)
3.5
1.5
-0.5
-2
Distrance (km)
2
Velocities (mm/yr)

Figure 5.

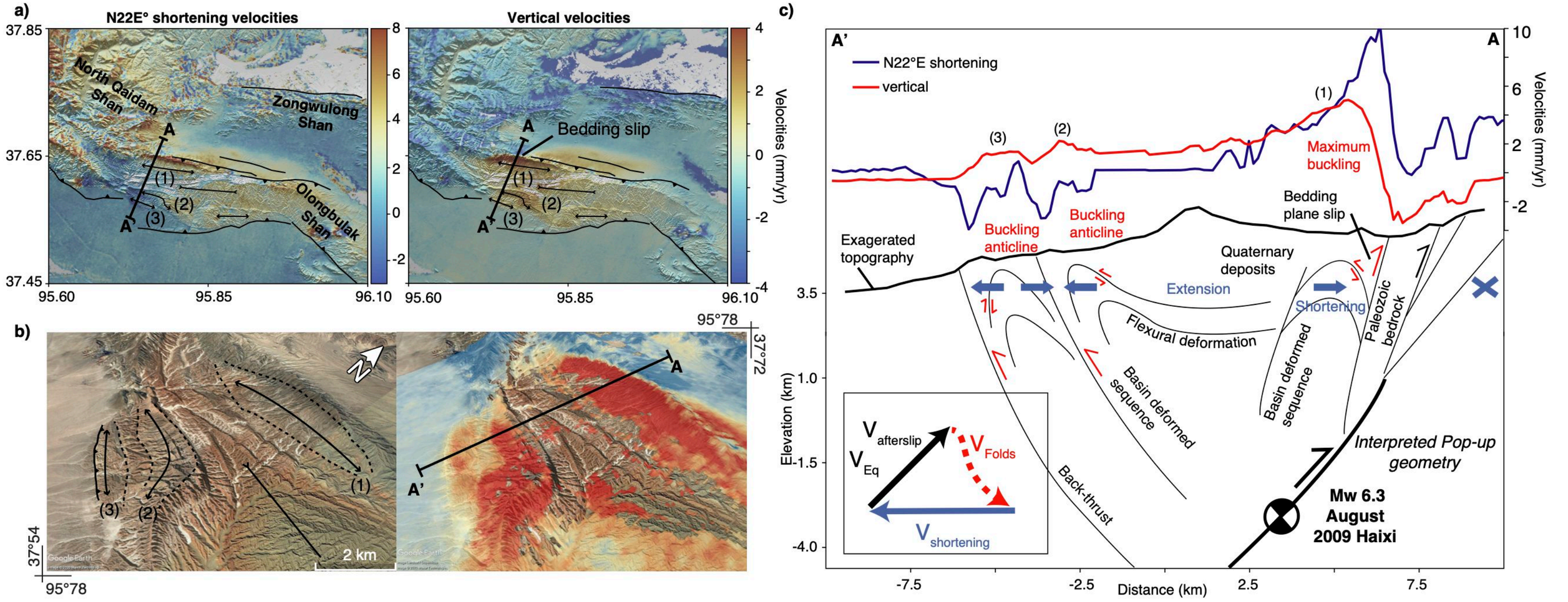
a)
N22E° shortening velocities
Vertical velocities
North Qaidam Shan
Zongwulong Shan
Olongbulak Shan
Bedding slip
A
A'
(1)
(2)
(3)
37.85
37.65
37.45
95.60
95.85
96.10
Velocities (mm/yr)
b)
95°78
37°72
37°54
2 km
c)
N22°E shortening
vertical
Maximum buckling
Buckling anticline
Bedding plane slip
Exagerated topography
Quaternary deposits
Extension
Shortening
Flexural deformation
Basin deformed sequence
Paleozoic bedrock
Back-thrust
Interpreted Pop-up geometry
Mw 6.3
August
2009 Haixi
V afterslip
V Eq
V Folds
V shortening
Elevation (km)
Distance (km)